Earth and Planetary Science Letters 386 (2014) 161–174

Contents lists available at ScienceDirect

Earth and Planetary Science Letters

www.elsevier.com/locate/epsl

Variable exhumation rates and variable displacement rates: Documenting recent slowing of Himalayan shortening in western Bhutan

Nadine McQuarrie [a,*,1], Tobgay Tobgay [b], Sean P. Long [c], Peter W. Reiners [d], Michael A. Cosca [e]

[a] Department of Geology and Planetary Science, University of Pittsburgh, Pittsburgh, PA 15260, USA
[b] Department of Geological Sciences, University of Texas, El Paso, TX 79968, USA
[c] Nevada Bureau of Mines and Geology, University of Nevada, Reno, NV 89557, USA
[d] Department of Geosciences, University of Arizona, Tucson, AZ 85721, USA
[e] United States Geological Survey, Denver Federal Center, MS 963, Denver, CO 80225, USA

ARTICLE INFO

Article history:
Received 8 March 2013
Received in revised form 24 October 2013
Accepted 25 October 2013
Available online 7 December 2013
Editor: M. Hirschmann

Keywords:
Himalaya
Bhutan
thermochronology
structural cross section
shortening rates

ABSTRACT

We link exhumational variability in space and time to the evolving geometry of the Himalayan fold–thrust belt in western Bhutan. By combining new and published geochronologic and thermochronologic data we document the burial age, peak temperatures and complete cooling history from 20 Ma to the present over an across-strike distance of ~125 km. These integrated cooling curves highlight windows of fast exhumation that vary spatially and temporally. We propose that pulses of fast exhumation are a result of structures that facilitate the vertical motion of material, illustrated in sequentially-restored cross sections. Due to a range of permissible geometries at depth, we explore and evaluate the impact of geometry on kinematics and rates of deformation. The linked cooling history and cross sections provide estimates of both magnitude and timing of thrust sheet displacement and highlight temporal variability in potential shortening rates. Structural and chronologic data illustrate a general north to south progression of Himalayan deformation, with emplacement of the Main Central thrust (MCT), Paro thrust and Shumar thrust by 12 to no later than 9 Ma. Two different geometries and kinematic scenarios for the Lesser Himalayan duplex are proposed. A north to south propagating duplex system requires that the southern portion of that system, south of the MCT, deformed and cooled by 9 Ma, leaving only the southernmost thrust sheets, including the Main Boundary and Main Frontal thrusts, to deform between 9 and 0 Ma. This limited post 9 Ma shortening would necessitate a marked slowdown in convergence accommodated on the Main Himalayan thrust. A two-tiered duplex system, which allows for the Paro window duplex and the southern Baxa duplex to form simultaneously, permits duplex formation and accompanying exhumation until 6 Ma. Limited cooling from ~200 °C to the surface post 6 Ma suggests either a decrease in shortening rates from 6 to 0 Ma or that duplex formation and exhumation are temporally decoupled. Our combined cooling curves highlight that the youngest cooling ages may not mark the fastest thrusting rates or the window of fastest exhumation. Instead, temporal variations in exhumation are best viewed through identifying transients in exhumation rate. We suggest that the strongest control on exhumation magnitude and variability is fold–thrust belt geometry, particularly the locations and magnitudes of footwall ramps, which can change over 10's of km distance. Balanced cross sections predict the location and magnitude of these ramps and how they vary in space and time, providing an untapped potential for testing permissible cross-section geometries and kinematics against measured cooling histories.

1. Introduction

Thermochronology allows utilization of a suite of minerals to determine the timing and rates over which rocks cool from higher (>450 °C) to lower (60 °C) temperatures (Naeser et al., 1989; Parrish, 1983; Hames and Bowring, 1994; Kirschner et al., 1996; Farley, 2000; Reiners et al., 2004, 2005; Harrison et al., 2009). In compressional orogens it is unclear how much of this temperature–time path is a function of active folding and faulting, or erosional processes that continue after folding and faulting have ceased. Because of uncertainty in how cooling ages are

* Corresponding author.
E-mail address: nmcq@pitt.edu (N. McQuarrie).
[1] Tel.: +412 624 8870; fax: +412 624 3914.

0012-821X/$ – see front matter
http://dx.doi.org/10.1016/j.epsl.2013.10.045

linked to fault displacement, particularly in fold–thrust belts where multiple generations of structures deform and/or transport a package of rocks, accurate assignment of an age and rate to thrust displacement is an ongoing challenge. We propose that the exhumation history of rocks may preserve periods of fast exhumation that can be linked to vertical motion of material over ramps, because cooling ages are most sensitive to the vertical (1D exhumation) component of the kinematic field, particularly when exhumation rates are high (e.g., Whipp et al., 2007). Calculating the rate of exhumation between closure temperatures of individual mineral systems (e.g., Thiede et al., 2009) can identify periods of fast exhumation. Linking periods of burial and slow or rapid exhumation to sequentially-restored cross sections illustrates and quantifies the magnitude of thrusting necessary to bury and exhume rocks, and allows correlation of periods of rapid exhumation to the structures that facilitated them (Long et al., 2012; Robinson and McQuarrie, 2012).

The Himalayan orogen is the result of continual collision between India and Asia that began at ca. 50 Ma (e.g., Hodges, 2000). Currently, shortening in the Himalaya is estimated to take up approximately one-third of the 5.8 ± 0.4 cm/yr India–Asia convergence rate (e.g., Bilham et al., 1997; Larson et al., 1999; Zhang et al., 2004; Bettinelli et al., 2006). Due to the difficulty in determining the exact age of displacement on individual thrust faults, documented rates of thrusting through the Himalaya are: (1) long-term shortening rates, determined by dividing the total amount of shortening by the age of initial motion on the Main Central thrust (MCT, ~25–20 Ma; $\sim 20 \pm 2.0$ mm/yr, e.g., DeCelles et al., 2001), (2) modern rates calculated via geodesy (19 ± 2.5 mm/yr; Bettinelli et al., 2006) or (3) Quaternary rates based on deformed Holocene river terraces (21.5 ± 2 mm/yr; Lavé and Avouac, 2000). Due to similarities between these long- and short-term shortening rates, a commonly held assumption is that Himalayan shortening rates have remained constant through time (e.g., Herman et al., 2010). Support for constant shortening rates may be found in the migration history of the foreland basin (e.g., Lyon-Caen and Molnar, 1985), which records the underthrusting of the Indian plate (Avouac, 2003). Although most of the data fit constant rates between 10 and 20 mm/yr, the spatial and temporal spread of data combined with imprecise age constraints allow for the data to also fit a wide variety of rates that vary significantly in both space and time. Recent studies linking sequentially-restored cross sections to all available timing constraints on the initiation and growth of structures have highlighted significant temporal variability in thrust displacement and overall shortening rates (Long et al., 2012; Robinson and McQuarrie, 2012; Tobgay et al., 2012). The most significant change highlighted by these studies is a slowing of thrusting on the basal décollement of Himalayan deformation, the Main Himalayan thrust (MHT), from ~10 Ma to the present.

In this paper we present a suite of geochronologic and thermochronologic data from western Bhutan that facilitate construction of temperature–time paths from ~750–800 °C to ~20 °C. This cooling history is linked to three different solutions for cross-section geometry and kinematics to evaluate the control that geometry has on the measured cooling history. Integrating exhumation timing and magnitude with sequentially-restored balanced cross sections predicts a range of potential shortening rates, and illustrates how they may vary through time.

2. Geologic background

2.1. Tectonostratigraphy

The Himalaya are divided into several tectonostratigraphic zones bounded by major brittle faults and ductile shear zones that can be recognized along the entire length of the orogen (Gansser, 1964, 1983; LeFort, 1975; Hodges, 2000; Yin, 2006). From south to north, the tectonostratigraphic subdivisions and major bounding faults include the Indo-Gangetic foreland basin, the Main Frontal thrust (MFT), Subhimalayan rocks (Siwalik Group), the Main Boundary thrust (MBT), Lesser Himalayan (LH) rocks, the Main Central thrust (MCT), Greater Himalayan (GH) rocks, the Southern Tibetan Detachment system (STDs), and overlying Tethyan Himalayan (TH) rocks (Fig. 1). Lesser Himalayan (LH) section is commonly divided into Lower LH rocks that are Paleo-Mesoproterozoic in age, and Upper LH rocks that are Neoproterozoic and younger (Gehrels et al., 2011; McQuarrie et al., 2013). Details on the lithologic characterization of map units presented here are discussed in McQuarrie et al. (2013).

2.2. Structure of western Bhutan

While the MFT is easily recognized in eastern Bhutan as the contact between the Miocene–Pliocene Siwalik Group and Quaternary foreland basin sediment, the location of the MFT in western Bhutan is less obvious. With much of the frontal part of the thrust belt covered by Quaternary sediment, the position of the MFT in western Bhutan is inferred from the southern boundary of uplifted fluvial terraces mapped by Gansser (1983). This places the MFT about 10 km south of the southernmost exposure of LH rocks (Fig. 1B). The subsurface dip of the MFT is inferred to be parallel to the orientation of nearby Siwalik Group rocks that strike E–W and dip between 30–50°N (Gansser, 1983; Long et al., 2011a).

The exact location of the MBT in western Bhutan is also uncertain. Across central and eastern Bhutan, the MBT is mapped as the contact between the upper Siwalik Group and upper LH rocks (Baxa Group) (Long et al., 2011a). In westernmost Bhutan, the Siwaliks and part of the Baxa Group are not exposed. The position of the MBT is extrapolated from the Siwaliks–Baxa contact east of Phuentsholing to the southern limit of exposed Baxa Group strata ~10 km west of Phuentsholing (Fig. 1B). Bedding and foliation in the Baxa Group generally strike E–W and dip N with dips ranging between 25° and 50°. The map view extent of the Baxa Group is much greater than its estimated thickness of 1.3 km. Faults within the Baxa Group were recognized in the field by both stratigraphic (lithologic repetition) and structural observations (localized zones of deformation, including highly-sheared and folded rocks, brecciation, and the presence of hot springs and tufa precipitation). These focused zones of high deformation separate continuous sections of significantly less deformed rocks. Baxa Group quartzite contains ubiquitous cross bedding, indicating right-side-up bedding orientations.

The contact between the Baxa Group and structurally-higher but older lower LH rocks (Daling–Shumar Group) is the Shumar thrust (ST). Bedding and foliation of rocks in the hanging wall of the thrust are parallel to those in the footwall. In addition, foliation is approximately parallel to bedding as indicated by the preservation of original sedimentary structures and bedding planes.

The MCT is exposed in multiple locations from north to south across western Bhutan (Tobgay et al., 2010; Tobgay et al., 2012). In the south, the MCT is mapped as the contact between the upper LH Jaishidanda Formation and structurally-overlying GH rocks. This contact approximates the maximum southern extent of the MCT, which is exposed only 15 km north of the MBT. In the north, the MCT is identified in a large erosional window that exposes GH rocks over the upper LH Paro Formation (Tobgay et al., 2010) (Fig. 1B). Field measurements of tectonic foliation show that GH rocks are parallel to bedding and foliation in the underlying Jaishidanda and Paro Formations. The southern extent of the Paro Formation is located in a narrow structural window near Chukha (Fig. 1B). The northern boundary of this exposure is a N-dipping, low-angle shear zone that places GH rocks over the Paro

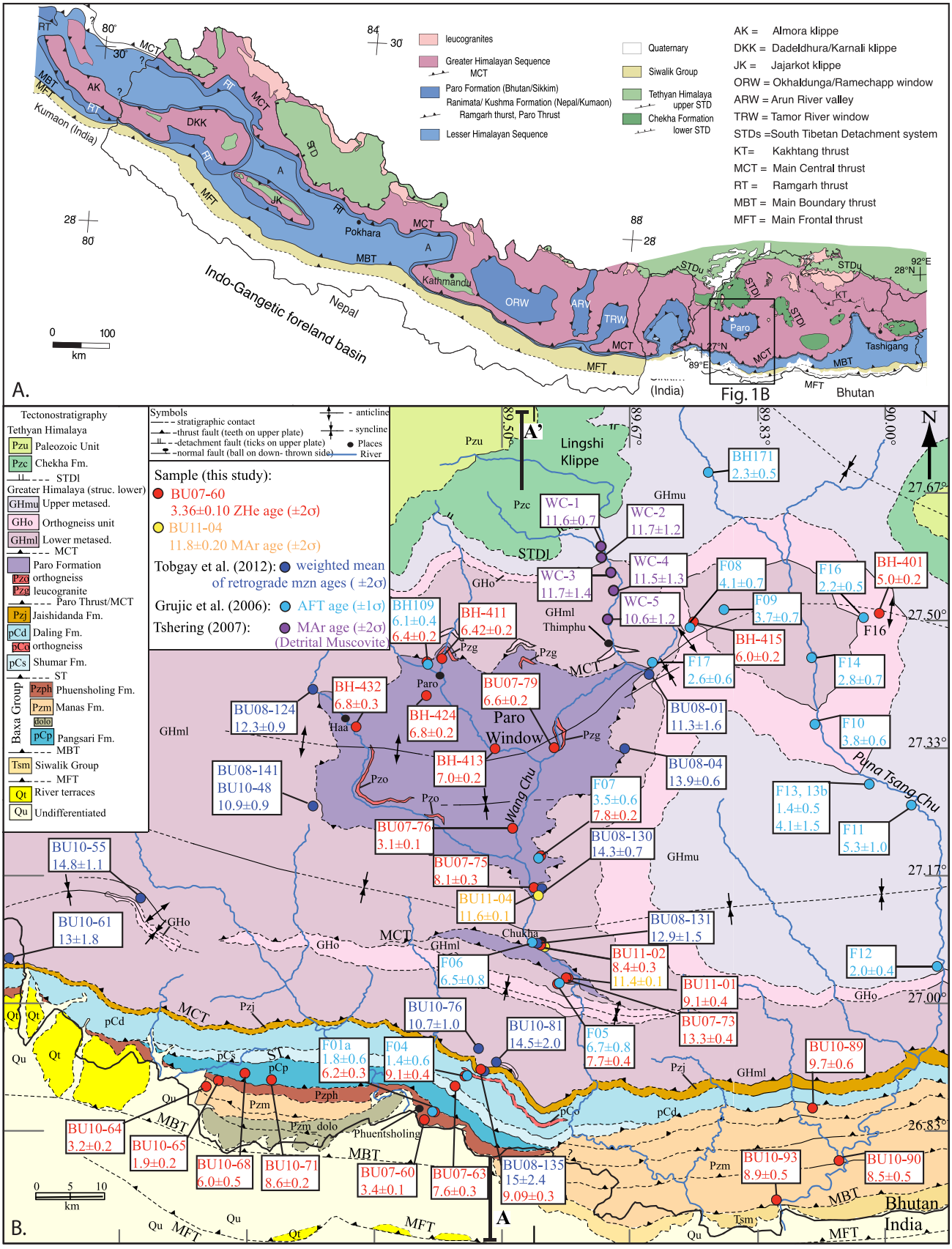

Fig. 1. A. Simplified geologic map of the Nepal and Bhutan portions of the Himalayan orogen modified from McQuarrie et al. (2008). Location of Fig. 1B is shown. B. Geologic map of western Bhutan modified from Tobgay et al. (2010) and Long et al. (2011a). A–A′ and partial lines mark the line of section for the Wang Chu cross section in Fig. 2. Circles mark locations of thermochronology samples from this study; yellow and red circles are MAr ages and ZHe ages respectively. Dark blue circles are monazite ages from Tobgay et al. (2012), light blue circles are AFT ages from Grujic et al. (2006), and purple circles are detrital MAr ages from Tshering (2007). Map projection is geographic lat/long (WGS84). (For interpretation of the references to color in this figure legend, the reader is referred to the web version of this article.)

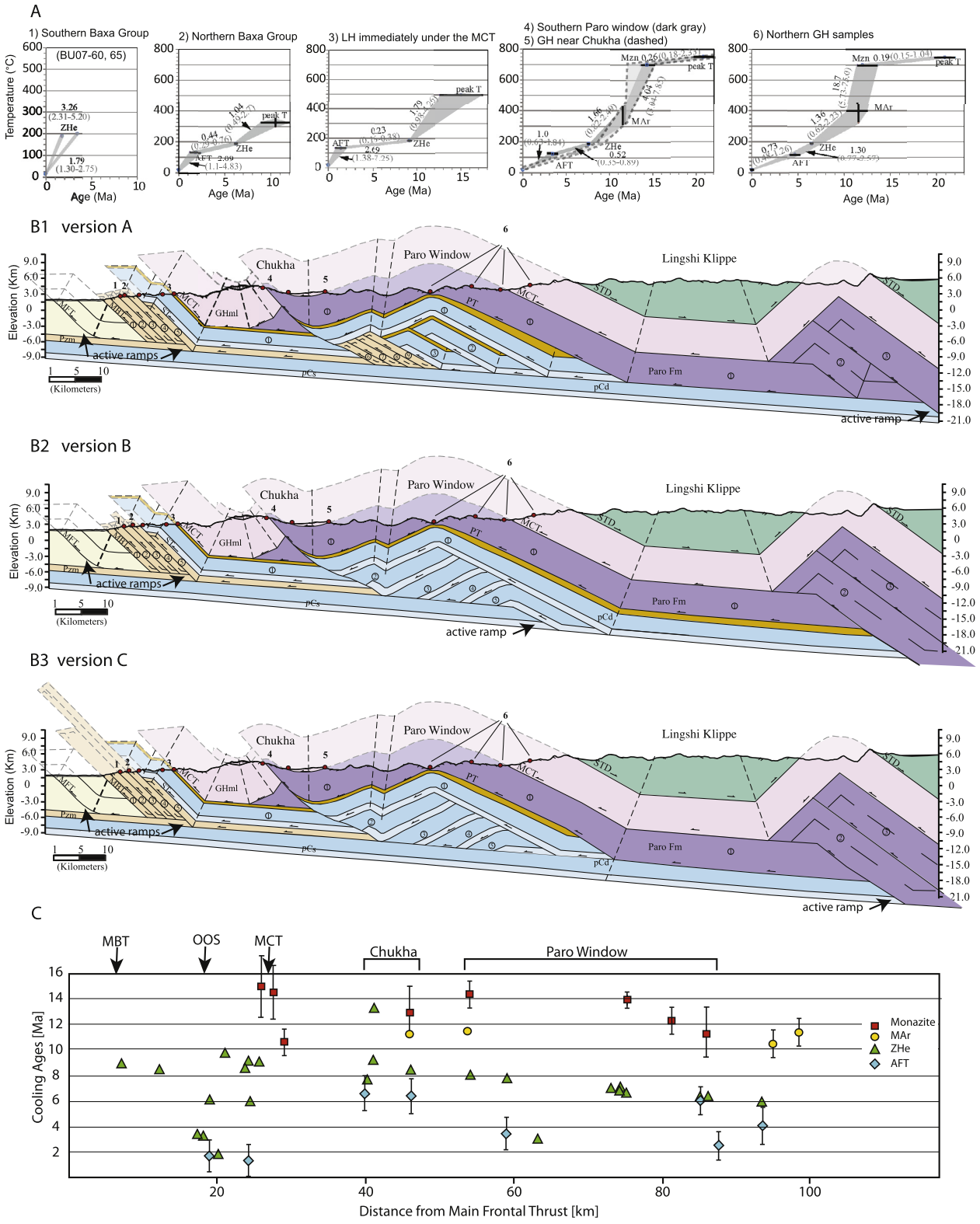

Fig. 2. A. Temperature–time (T–t) paths for representative samples are linked to their respective sample locations on the cross sections (B). The gray swath illustrates variability between successive T–t data points and accounts for ranges of timing and magnitude of peak temperature, ranges of closure temperature, and cooling age uncertainty. Black numbers indicate exhumation rates (mm/yr) for a 30 °C/km geothermal gradient, and gray numbers indicate the permissible range of exhumation rates for given age uncertainties, closure temperature ranges, and modeled geothermal gradients (20 and 40 °C/km). B. Three versions of the Wang Chu balanced cross-section in western Bhutan; line of section and unit abbreviations shown on Fig. 1. Translucent areas represent rock that has passed above the modern erosion surface. Locations of thermochronology samples from this study (red circles) are shown. Horses in the LH duplexes are numbered in the order in which they were emplaced. C. Cooling ages plotted with respect to map distance from the MFT. Brackets indicate region of Chukha and Paro Window. Arrows indicate location of MBT, MCT and a proposed out-of-sequence (OOS) thrust to account for younger ages and buried foreland. (For interpretation of the references to color in this figure legend, the reader is referred to the web version of this article.)

Formation, while the southern boundary is a discrete, brittle fault dipping ~45°N that places the Paro Formation over GH rocks.

South of Chukha region, GH foliation has been folded into a regional anticline–syncline pair (Figs. 1 and 2). The fault that places the Paro Formation over GH rocks at the southern window is along strike, and east of the anticline axis (Long et al., 2011a). The syncline limits the southern-most extent of the Paro Formation at depth (Fig. 2), and constrains the shallowest depth to the regional décollement in western Bhutan. At the axial zone of the syncline a total thickness of 7.5 km of GH rocks, as well as the entire thickness of the Jaishidanda Formation, Daling–Shumar Group, and Baxa Group must fit above the basal dècollemont (Fig. 2).

Based on the first-order geometry of the Himalayan fold–thrust belt described above, the minimum depth to the basal décollement for western Bhutan is approximately at the stratigraphic top of the Daling Formation, which is ~6 km deep in the foreland and dips 4°N (Hauck et al., 1998; Mitra et al., 2005; Schulte-Pelkum et al., 2005). This depth and broad geometry of the MHT matches previous predictions made using receiver function analyses, earthquake focal mechanisms and reflection seismology (Ni and Barazangi, 1984; Hauck et al., 1998; Schulte-Pelkum et al., 2005). Both receiver function analyses and reflection seismology show the décollement steepening north of the STDs exposed in the Lingshi Klippe (Hauck et al., 1998; Schulte-Pelkum et al., 2005) (Fig. 1). Whether the décollement in western Bhutan steepens at this location is uncertain due to the separation of our study area from the geophysical studies by the Yadong cross structure, a down-to-the-west normal fault (Wu et al., 1998). Two of our proposed balanced cross sections indicate a ramp at northern edge of the klippe (Fig. 2).

Because the MCT and underlying Paro Formation are folded into a broad dome (Fig. 1), deformed LH rocks must fill the space between the base of the Paro Formation and the basal decollement (McQuarrie et al., 2008; Bhattacharyya and Mitra, 2009; Mitra et al., 2010; Long et al., 2011b). This space can be filled by either repeating thrust sheets of the Baxa Group (Tobgay et al., 2012), the Daling–Shumar Group, or by repeating a combination of Baxa Group and Daling–Shumar Group thrust sheets. We explore: (1) a combined upper and lower LH duplex based on the duplex geometry exposed to the east and west (Bhattacharyya and Mitra, 2009; Mitra et al., 2010; Long et al., 2011b) and (2) a lower LH only geometry (Fig. 2). The Baxa Group only geometry in Tobgay et al. (2012) increases the amount of shortening in the duplex by 34 km and implies the same kinematics as the combined upper and lower LH duplex.

3. Thermochronology and geochronology

3.1. Monazite data

Monazite growth and chemistry in metapelitic rocks are a function of reactions involving silicate minerals, particularly garnet (Kohn and Malloy, 2004; Pyle et al., 2001; Spear and Pyle, 2002; Wing et al., 2003). During burial of rocks, monazite grows over a wide range of temperatures. During prograde monazite and garnet growth, yttrium (Y) is preferentially incorporated into garnet, leaving the monazite low in Y. During partial melting, existing monazite dissolves into the melt, while garnet continues to grow. Upon cooling and melt recrystallization, garnet dissolves and retrograde, high Y monazite grows either as new grains or as overgrowths on older grains (Kohn et al., 2004). *In situ* Th–Pb geochronology of metamorphic monazite combined with geochemical mapping identified both prograde and retrograde monazite ages across western Bhutan (Tobgay et al., 2012). Prograde monazite ages from western Bhutan indicate that GH rocks were undergoing structural burial from 26 to ~21 Ma (Tobgay et al., 2012; Kellett et al., 2010), while the retrograde ages argue for crystallization of *in situ* melts from 15 to 9.5 Ma. In this study we compile the young retrograde ages from GH rocks to identify the time of cooling through ~700 °C, the approximate minimum temperature for muscovite dehydration-melting (Spear et al., 1999; Pyle and Spear, 2003; Kohn et al., 2005) (Table 1). Another critical age constraint is from a prograde (burial) LH monazite growth age from the Jaishidanda Formation immediately under the MCT (Fig. 1). This data requires the LH rocks at this location to be buried by the overriding MCT sheet at 15 ± 2.4 Ma (Tobgay et al., 2012).

3.2. White Mica $^{40}Ar/^{39}Ar$ data

We obtained 2 new white mica $^{40}Ar/^{39}Ar$ ages (MAr) from GH rocks in the immediate hanging wall of the MCT (BU11-04 and BU11-02; Fig. 1, Table 1). Analyses were performed at the USGS geochronology laboratory in Denver (see Supplementary Material [SM] Methods). BU11-04 yielded a cooling age of 11.7 ± 0.1 Ma while sample BU11-02 yielded an age of 11.4 ± 0.1 Ma. In addition we compile 5 detrital MAr ages on white mica from Tshering (2007). These samples were collected along the Wang Chu valley, north of the Paro window (Fig. 1B). Although ages for individual mica grains range between 14.0 ± 0.1 Ma and 9.4 ± 0.1 Ma, the combined probability density function (PDF) for all samples shows a single strong peak at 11.4 ± 1.5 Ma. These data suggest that GH rocks cooled through the MAr closure temperature (~350°–450 °C) at about 11.5 Ma both north and south of the Paro window.

3.3. Zircon (U–Th)/He data

We present 27 new zircon (U–Th)/He ages (ZHe) from 23 LH samples and 4 GH samples (Fig. 1; Table 1). Analyses were performed at the University of Arizona Radiogenic Helium Dating Laboratory (see SM Methods). Each age represents a weighted mean age of 1 to 3 single zircon grains and is reported with 2σ analytical error (Table 1; Fig. 1). Single-grain ZHe ages and supporting data are shown in Table SM2.

Two GH samples were collected northeast of the Paro window (BH-415 and BH-401) and two samples were collected south of the Paro window (BU11-02, F05). The northern samples yielded ages of 5.0 ± 0.2 and 6.0 ± 0.2 Ma, respectively, whereas the southern samples yielded older cooling ages of 8.4 ± 0.3 Ma (BU11-02) and 7.6 ± 0.3 Ma (F05).

Eleven samples were analyzed from the LH Paro Formation. The northern six samples cluster around 6.6 Ma, with ages ranging from 6.4 ± 0.2 (BH-109), 6.4 ± 0.2 (BH-411), 6.6 ± 0.2 (BU07-79), 6.8 ± 0.2 (BH-424), 6.9 ± 0.3 (BH-432), and 7.0 ± 0.2 Ma (BH-414). The southern three samples show one young age of 3.1 ± 0.1 Ma (BU07-76) and two similar ages of 8.1 ± 0.3 (BU07-75) and 7.8 ± 0.4 Ma (F07). Two samples from the southern Paro window (south of Chukha) yielded 9.1 ± 0.4 Ma (BU11-01) and 13.3 ± 0.4 Ma (BU07-73) cooling ages.

Twelve samples were analyzed from LH rocks exposed in southernmost Bhutan. Baxa Group samples near the town of Phuentsholing and to the west produced very young ages: 1.9 ± 0.2 (BU10-65), 3.2 ± 0.2 (BU10-64) and 3.4 ± 0.1 Ma (BU07-60), with one sample at 6.2 ± 0.3 Ma (F01a). Baxa Group samples to the east of Phuentsholing are notably older with ages of 8.5 ± 0.5 (BU10-90), 8.8 ± 0.5 (BU10-93), and 9.7 ± 0.6 Ma (BU10-89). Rocks sampled from the Baxa Group, Daling–Shumar Group and Jaishidanda Formation north of Phuentsholing also yield older cooling ages, 6.0 ± 0.5 (BU10-68), 7.6 ± 0.3 (BU07-63), 8.6 ± 0.2 (BU10-71), 9.1 ± 0.3 (BU08-135), and 9.3 ± 0.4 Ma (F04).

Table 1
Sample locations and cooling ages from western Bhutan.

Sample	Longitude (dd.ddddd)	Latitude (dd.ddddd)	Elevation (m)	Map unit	Lithology	MAr age (Ma)	MAr 2σ error (Ma)	ZHe age (Ma)	ZHe 2σ error (Ma)	# of zircons analyzed	AFT age (Ma)	AFT 1σ error (Ma)	Youngest Mnz rim age (Ma)	Mnz rim 2σ error (Ma)
BU07-60	89.39319	26.85456	355.0	Phuentsholing	quartzite	–	–	3.36	0.10	1	–	–	–	–
BU07-63	89.43622	26.89172	1200.0	Daling Fm.	quartzite			7.64	0.32	2				
BU07-73	89.58050	27.02925	1895.0	Paro	quartzite	–	–	13.26	0.42	3	–	–	–	–
BU07-75	89.54175	27.15200	2265.0	Paro	quartzite	–	–	8.05	0.26	3	–	–	–	–
BU07-76	89.51678	27.22606	2020.0	Paro	quartzite	–	–	3.06	0.08	1	–	–	–	–
BU07-79	89.57497	27.33758	2188.0	Paro	quartzite	–	–	6.60	0.20	3	–	–	–	–
BU08-01	89.69115	27.42667	2615.0	GHS	paragneiss	–	–	–	–	–	–	–	10.30	1.00
BU08-04	89.65653	27.32392	2996.0	GHS	paragneiss	–	–	–	–	–	–	–	13.30	0.40
BU08-124	89.25842	27.40536	2780.0	GHS	paragneiss	–	–	–	–	–	–	–	12.00	0.80
BU08-130	89.54369	27.14997	2265.0	GHS	paragneiss	–	–	–	–	–	–	–	13.40	0.60
BU08-131	89.55766	27.06505	1545.0	GHS	paragneiss	–	–	–	–	–	–	–	12.40	1.20
BU08-135	89.46922	26.91692	1865.0	Jaishidanda	quartzite	–	–	9.09	0.30	3	–	–	15.00	2.40
BU08-141	89.26180	27.25369	3715.0	GHS	orthogneiss	–	–	–	–	–	–	–	9.50	0.80
BU10-48	89.26336	27.52803	3715.0	GHS	paragneiss	–	–	–	–	–	–	–	11.70	2.20
BU10-55	89.02656	27.13889	2310.0	GHS	paragneiss	–	–	–	–	–	–	–	14.80	1.10
BU10-61	88.89622	27.04997	840.0	GHS	schist	–	–	–	–	–	–	–	11.50	2.00
BU10-64	89.11122	26.89972	590.0	Manas	quartzite	–	–	3.24	0.16	3	–	–	–	–
BU10-65	89.12011	26.90158	945.0	Phuentsholing	phyllite	–	–	1.86	0.20	2	–	–	–	–
BU10-68	89.14875	26.89614	1370.0	Pangsari	quartzite	–	–	6.03	0.26	2	–	–	–	–
BU10-71	89.20083	26.89519	1595.0	Pangsari	quartzite	–	–	8.58	0.24	1	–	–	–	–
BU10-76	89.47106	26.94322	1625.0	GHS	paragneiss	–	–	–	–	–	–	–	10.70	1.00
BU10-81	89.49167	26.92267	2000.0	GHS	paragneiss	–	–	–	–	–	–	–	14.50	2.00
BU10-89	89.90786	26.85717	880.0	Baxa	quartzite	–	–	9.74	0.6	2	–	–	–	–
BU10-90	89.94411	26.79442	198.0	Baxa (Jainti)	quartzite	–	–	8.54	0.52	3	–	–	–	–
BU10-93	89.86333	26.74447	140.0	Baxa	quartzite	–	–	8.93	0.52	2	–	–	–	–
BU11-01	89.58273	27.02924	1860.0	GHS	paragneiss			9.06	0.36	3				
BU11-02	89.55650	27.06630	1545.0	GHS	paragneiss	11	0.07	8.35	0.26	3				
BU11-04	89.54356	27.14964	2255.0	GHS	paragneiss	11.66	0.20	–	–	–	–	–	–	–
BH-411	89.41996	27.46156	2335	GHS	paragneiss			6.42	0.22	3				
BH-424	89.42762	27.38741	2274	Paro	quartzite			6.8	0.22	3				
BH-432	89.30901	27.36241	3042	Paro	quartzite			6.87	0.26	3				
BH-413	89.47229	27.34339	2182	Paro	quartzite			6.99	0.22	3				
BH-415	89.74973	27.49078	3123	GHS	orthogneiss			6.03	0.2	3				
BH 401	89.99908	27.50400	1483	GHS	orthogneiss			5.03	0.16	3				
MAr samples from Tshering (2007)														
WC-1	89.63000	27.59450	2600.0	GHS	detrital muscovite	11.61	0.66							
WC-2	89.63150	27.58880	2587.0	GHS	detrital muscovite	11.73	1.24							
WC-3	89.63880	27.57280	2502.0	GHS	detrital muscovite	11.74	1.44							
WC-4	89.64980	27.53630	2425.0	GHS	detrital muscovite	11.51	1.31							
WC-5	89.64120	27.50070	2335.0	GHS	detrital muscovite	10.57	1.16							
AFT samples from Grujic et al. (2006); ZHe from this study														
BH299	89.33608	27.79572	4729.0	GHS	gneiss	–	–	–	–	–	4.4	0.5	–	–
BH109	89.39972	27.44222	2400.0	Paro	quartzite	–	–	6.4	0.22	3	6.1	0.4	–	–
F01a	89.40906	26.86218	644.0	Phuentsholing	quartzite	–	–	6.22	0.26	2	1.8	0.6	–	–
F04	89.45933	26.90723	1751.0	Daling Fm.	orthogneiss	–	–	9.15	0.36	3	1.4	0.6	–	–
F07	89.55243	27.18909	2153.0	Paro	quartzite	–	–	7.7	0.36	2	3.5	0.6	–	–
F06	89.55721	27.06583	1545.0	GHS	gneiss	–	–	–	–	–	6.5	0.8	–	–
F05	89.57415	27.02737	1881.0	GHS	paragneiss	–	–	7.66	0.26	3	6.7	0.8	–	–
F17	89.69520	27.44172	2524.0	GHS	paragneiss	–	–	–	–	–	2.6	0.6	–	–
F08	89.74884	27.49029	3113.0	GHS	gneiss	–	–	–	–	–	4.1	0.7	–	–
BH171	89.77081	27.69294	1440.0	GHS	migmatite	–	–	–	–	–	2.3	0.5	–	–
F09	89.79600	27.51240	1953.0	GHS	gneiss	–	–	–	–	–	3.7	0.7	–	–
F14	89.90648	27.45064	1192.0	GHS	gneiss	–	–	–	–	–	2.8	0.7	–	–
F10	89.91159	27.36351	1044.0	GHS	gneiss	–	–	–	–	–	3.8	0.6	–	–
F16	89.96202	27.50643	1399.0	GHS	Augen gneiss	–	–	–	–	–	2.2	0.5	–	–
F13	89.98610	27.29079	881.0	GHS	paragneiss	–	–	–	–	–	1.4	0.5	–	–
F13b	89.98610	27.29079	881.0	GHS	paragneiss	–	–	–	–	–	4.1	1.5	–	–
F11	90.03697	27.26311	710.0	GHS	pegmatite	–	–	–	–	–	5.3	1.0	–	–
F12	90.07618	27.03204	361.0	GHS	gneiss	–	–	–	–	–	2.0	0.4	–	–

3.4. Apatite fission track data

Apatite fission track (AFT) ages for western Bhutan samples were presented in Grujic et al. (2006). While AFT ages from western Bhutan are generally younger than those to the east (e.g., Grujic et al., 2006), AFT ages along our cross-section line through the Paro window are quite variable and range from 1.4 ± 0.1 to 6.7 ± 0.1 Ma. AFT ages in the southern-most exposure of LH rocks near Phuentsholing are the youngest (1.4–1.8 Ma), while those exposed to the north in the two Paro window exposures are older (6.0–6.7 Ma), with one sample at 3.5 Ma. The Pliocene ages in western Bhutan that suggest more efficient erosion west of the Shillong plateau (Grujic et al., 2006) are focused along the Puna Tsang Chu valley, ~35–50 km to the east of the Paro window (Fig. 1).

4. Transient temperature–time paths

Transients in the exhumation history are periods when exhumation was notably slower or faster than a longer-term average rate. We postulate that the most straightforward way to generate spatially- and temporally-varying periods of rapid exhumation is through relatively rapid erosion accompanying the motion of thrust sheets over footwall ramps or the construction of duplexes (i.e., the stacking of footwall ramps, underplating or accretion). Thus when the exhumation rate diminishes, it signifies that region is no longer the site of active ramps or underplating and it is simply translated along the decollement. We quantify transient exhumation by correcting the predicted higher temperature exhumation rate with rates predicted by lower temperature samples (e.g., Ehlers et al., 2003; Thiede et al., 2009). Thus, instead of reporting the time-averaged rates based on sample closure ages to the present, we report a series of exhumation rates between closure of individual thermochronologic systems (Table SM3).

We generated temperature–time (T–t) paths that quantify time-averaged exhumation rates for our samples through 1-D thermal modeling (e.g., Laslett et al., 1987; Mancktelow and Grasemann, 1997; Ehlers and Farley, 2003; Thiede et al., 2009) using the AGE2EDOT program (Brandon et al., 1998). AGE2EDOT models the permissible range of exhumation rates required to obtain the observed MAr, ZHe, and AFT ages, as well as a permissible range of closure temperatures for each thermochronologic age. Support for a 1-D thermal modeling approach comes from Whipp et al. (2007), who found that cooling ages are the most sensitive to the vertical (i.e., 1-D exhumation) component of the kinematic field in rapidly eroding orogens. Although this approach does not capture all of the details of the evolving thermal field, it provides a rationale for placing cooling ages in the context of a sequentially-restored cross section. The sequential reconstruction suggests windows of time and space where significant structural elevation was generated (e.g., Robinson and McQuarrie, 2012).

We based estimates for thermal diffusivity and internal heat production on values previously estimated for Himalayan rocks (Ray et al., 2007; Whipp et al., 2007; Herman et al., 2010). Initial conditions that were held constant include the depth to constant temperature, and average annual surface temperature. The geothermal gradient measured at the surface was the largest variable in the 1-D modeling. Because data quantifying modern geothermal gradients in Bhutan are not available, we used geothermal gradients of 20, 30, and 40 °C/km to cautiously account for the effects of widely ranging geothermal gradients (e.g., Long et al., 2012). The modeled closure temperature ranges for MAr, ZHe, and AFT ages varied between 324 and 400 °C, between 186 and 203 °C, and between 117 and 136 °C, respectively (Table SM3).

We used the published monazite data to estimate the age that peak temperatures were reached (prograde chemistry and age) and the age of crystallization of partial melt (retrograde chemistry and age) (Tobgay et al., 2012). For each T–t path, exhumation rates were calculated that incorporate the age of peak temperature, the age and temperature of each thermochronologic system, and the modern day surface conditions (20 °C at 0 Ma) using AGE2EDOT modeling results. We incorporate both the uncertainty in the age and the uncertainty in temperature based on the range in initial geothermal gradient (20–40 °C/km) used in the thermal modeling. We focused our T–t modeling on regions where we have the most complete thermal history. Fig. 2 shows the T–t paths linked to the locations of the samples on a balanced cross section. Gray swaths highlight the permissible variation in the T–t path. Medial exhumation rate (mm/yr) for a 30 °C/km geothermal gradient is shown in black text. Gray text indicates the permissible range in exhumation rates based on different initial geothermal gradients and uncertainty in age. Explanation of range of uncertainty in the T–t path is provided in SM methods.

4.1. Rapid cooling

Prograde (burial) monazite growth in GH rocks until 20.8 ± 1.1 Ma indicates the youngest possible time for achievement of peak temperatures of 750–800 °C (Daniel et al., 2003; Kohn, 2008; Tobgay et al., 2012). We propose that these high temperatures existed until at least 15.1 ± 0.4 Ma, which is the age of the oldest retrograde monazite ($n = 18$) from the base of the GH section, indicating that GH rocks remained above temperatures necessary for crystallization of partial melt (~700 °C) until 15 Ma (Tobgay et al., 2012). Retrograde monazite grew from 10.5 to 15.1 Ma, indicating that when and where rocks cooled below 700 °C varied spatially. North of Paro retrograde monazite grew from 10.5 to 13.3 Ma, while south of Paro ages are ~13–14 Ma (Fig. 1). Muscovite cooled below 325–400 °C at 11 Ma. The similar ages for both retrograde monazite growth and muscovite closure, particularly taking into account the range in cooling ages, requires incredibly fast exhumation from 700 to 400–325 °C that was broadly similar on both edges of the Paro Window. Corresponding exhumation rates range from 4.1 to 62.5 mm/yr for a 30 °C/km geothermal gradient with a total exhumation rate range of 3.0–93.7 mm/yr for 40 °C/km and 20 °C/km geothermal gradients, respectively. This period of very fast exhumation postdates motion on the STDs (Kellett et al., 2010), and potentially postdates motion on the MCT and Paro Thrust (PT) (Tobgay et al., 2012). ZHe ages from the Paro window region have a combined age of 6.5 ± 0.5 Ma in the north and 8.0 ± 0.4 Ma in the south. These ages suggest cooling rates of 0.8–2.3 mm/yr (0.6–3.4 mm/yr; parentheses mark total range in cooling rates) from ~400 °C to 190 °C. Although slower than the rapid cooling from 700–400 °C, permissible rates as high as 2–3 mm/yr suggests this region was still actively exhuming over this window of time.

Lower LH rocks exposed immediately beneath the MCT experienced peak temperatures of 500 °C and are associated with prograde monazite growth at 15 ± 2.4 Ma (Tobgay et al., 2012). From peak temperatures these rocks cooled quickly to 187–189 °C by 9.2 ± 0.2 Ma (ZHe) at rates of 1.3–2.8 mm/yr (1.0–4.3 mm/yr) (Fig. 2).

4.2. Slow cooling

AFT data through the Paro window region display a wide range of ages, between 2.6 and 6.7 Ma (Fig. 1). Our modeling indicates that this region continued to cool from 190 °C to 121–124 °C at rates of 0.5–1.7 mm/yr (0.4–2.6 mm/yr). This range is moderately slower than rates from ~400 to 190 °C, with the younger AFT ages requiring slower exhumation over this window of time. Exhumation rates to the present continued to slow to 0.5–0.8 mm/yr, with a total range of 0.3–1.3 mm/yr.

Lesser Himalayan rocks also show slow cooling from 9–6 Ma to 1.8–1.4 Ma. Lower LH rocks below the MCT underwent a dramatic decrease in cooling rates between 9 Ma and 1.4 Ma of 0.2–0.3 mm/yr (0.2–0.4 mm/yr), while Baxa Group rocks to the south show slow cooling from 6.2 Ma (ZHe) to 1.8 Ma (AFT) at 0.4–0.5 mm/yr (0.3–0.7 mm/yr) (Fig. 2).

4.3. Young rapid cooling

Young AFT ages and ZHe ages from rocks exposed along the northern edge of the Baxa Group require an increase in exhumation across a relatively narrow area over the last ~2 Myr. From ~2 Ma to present exhumation rates are 1.4–3.8 mm/yr (1.2–7.3 mm/yr).

5. Integrating pulses of rapid cooling with cross-section kinematics

The previous section identified periods of time of fast exhumation (rapid cooling from monazite to ZHe closure temperatures in the region of the Paro window), slow exhumation (cooling between ZHe and AFT closure temperatures around the Paro window and immediately south of the MCT) and very recent, ~2 Ma to present rapid exhumation of a few of the LH rocks within the southern Baxa duplex. Both the Paro window and a significant portion of the Baxa Group rocks to the south display ZHe ages between 6 and 9 Ma (Fig. 2). These "older" ZHe ages combined with relatively young (1–3 Ma) AFT ages highlight a window of time of minimal exhumation and thus limited duplex growth.

Prograde (burial) monazite growth in GH rocks until 20.8 ± 1.1 Ma indicates the oldest possible age for motion on the MCT, which initiates exhumation and thus inhibits prograde monazite growth. The prograde LH monazite age immediately under the MCT requires burial by the overriding MCT at 15 ± 2.4 Ma. Geometric relationships indicated by the map patterns require the MCT to completely override the Paro Formation and that the combined motion on the MCT and PT must be great enough to bury sample BU08-135 before ~12.6 Ma. This distance is a function of the geometry of the duplex and can range from 287 to 360 km, necessitating thrusting rates of 3.6–5.8 cm/yr (Fig. 3), which are indistinguishable from plate tectonic rates over this window of time (Copley et al., 2010). Rapid thrusting on the MCT from 20 to 15 Ma would be facilitated by partial melting of GH rocks over this time (Tobgay et al., 2012), leading to high strain rates localized by the presence of melt (Hollister and Crawford, 1986).

The first pulse of rapid cooling for the Paro window region was from 15 to 11 Ma (Fig. 2). This cooling could be initiated by continued motion on the MCT, and initiation of motion on the PT and ST (Fig. 3) and/or growth of the LH duplex under the Paro window. Motion over the footwall ramps of the PT and ST increased structural elevation by 6 and 4 km respectively (Fig. 2). The growth of the duplex under the Paro window increased structural elevation another 6–10 km. A significant decrease in cooling rate between the age of ZHe cooling and AFT cooling (Fig. 2) occurs at 9 Ma in the southern Paro window, and youngs to 6 Ma in the north. We argue that this decrease in cooling rate indicates cessation of duplex growth and translation along a footwall flat. The southern duplex comprised of Baxa Group rocks also indicates cooling through ZHe closure temperatures by 9 to 6 Ma, with a few samples indicating rapid exhumation from ~2 Ma to present. Rapid cooling in northern Bhutan north of the Lingshi klippe suggests that much of the structural elevation in that region must have been gained between ~13 and 9 Ma (Grujic et al., 2011; Warren et al., 2012, unpublished 9 Ma ZHe ages). The geometry of this structure is uncertain. Here we simply show it as a duplex of Paro Formation rocks that feeds slip into an out-of-sequence MCT.

A purely southward propagating duplex (Figs. 2B1, 3A) combined with 9–6 Ma cooling ages in the southern Baxa duplex requires almost all of the shortening in the system to predate 9 or 6 Ma. The abundance of ~9 Ma ZHe cooling ages in Baxa rocks combined with a ZHe cooling age of 8.9 ± 0.5 Ma (BU10-93) in the immediate hanging wall of the MBT argues for minimal exhumation and potentially minimal shortening post 9 Ma. An implication of this scenario is that the Paro duplex predates 9 Ma and would be a major contributor to the rapid cooling identified from 15 to 11 Ma. Cooling through ZHe closure temperatures indicates continued erosion after uplift had ceased. In contrast, a forward dipping duplex comprised of Daling–Shumar Group rocks under the Paro window allows for both duplexes (Paro window and Baxa) to grow simultaneously. Thus the 9 Ma ZHe age could indicate initiation of duplex formation while the 6 Ma cooling ages, particularly in the northern Paro duplex would indicate the end of duplex formation (Figs. 2B2, 2B3, 3B, 3C). By slightly changing the geometry of the Paro duplex, the kinematic implications of the cooling history can be altered. In one scenario the northern two horses in the Paro window are linked to shortening on the MBT and the MFT (Fig. 3B) post 6 Ma. This shortening and vertical uplift in the Paro region (4–5 km) would be less than that needed to cool through the ZHe closure temperature. Alternatively, the Paro duplex was completed at 6 Ma and simply translated along a decollement from 6 Ma to present (Fig. 3C). Version C requires no uplift of the Paro region post 6 Ma, but significantly more shortening (and potentially cooling) in the frontal Baxa Group rocks.

Linking these cooling, geometric and kinematic constraints allows us to calculate a range of different shortening rates for each version of the cross section (Figs. 3, 4). A 9 Ma ZHe age from the immediate hanging wall of the ST requires motion on this structure to be over by this time, however, it does not preclude earlier displacement. Using a range of ages for both emplacement of the PT (15–12 Ma) and cessation of duplex formation (9–6 Ma), permissible shortening rates during slip on the ST range from 13.3 to 52.6 mm/yr, and permissible rates for duplex formation range from 25.5 to 76 mm/yr. Combining ST age and displacement with that of the duplex is possible for cross-section version A (Fig. 3A). Here, average rates from 15–12 Ma to 6–9 Ma range from 21.5 mm/yr to 64.6 mm/yr.

The majority of duplex formation completed by 9–6 Ma necessitates significantly slower shortening rates from 6–9 Ma to present (Figs. 3, 4). These shortening rates range from 3.7 to 8 mm/yr with the lowest rates determined from version A and the fastest from version C. Since version C allows for the fastest recent rates, we explored the implications of constant shortening rates on the measured cooling ages. Constant shortening from initiation of the MCT at ~20 Ma to cessation of the ST at 9 Ma indicates rates of 31–37 mm/yr, while the remaining shortening from 9 Ma to present corresponds to a rate of 18.5 mm/yr. Using this long-term rate, significant structural elevation of the duplex is still being gained at 5 Ma (Fig. 3C_k). A constant shortening rate implies that a ~6 km increase in structural elevation had no impact on ZHe and possibly AFT ages.

Young, rapid exhumation in the middle of the southern duplex argues for a more rapid shortening rate and rejuvenation of a vertical component of the displacement field from 2 Ma to present (Fig. 2). This out of sequence thrusting also provides a mechanism for burying frontal structures, particularly the MFT. However, the resulting shortening associated with this recent motion can be as small as 7–10 km.

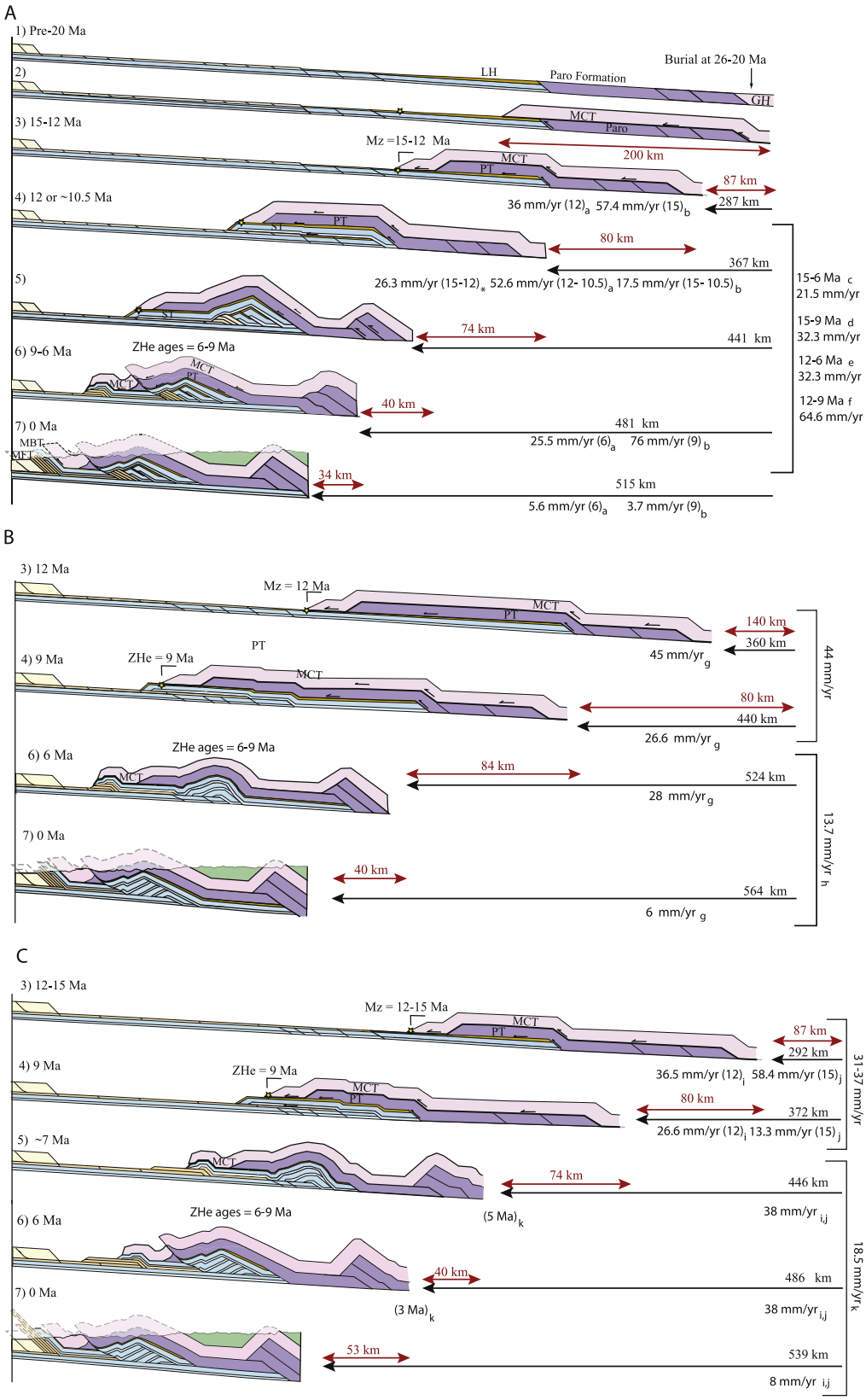

Fig. 3. Differing sequentially-restored kinematic scenarios for the Wang Chu cross section. Total shortening (black) and incremental shortening (red) indicated at each step. See Table 2 for summary of timing constraints and shortening magnitudes; no age constraints are available for increment 5. Step 7 is final cross-section geometry illustrated in Fig. 2. Subscript letters show potential variations in age (marked in parentheses) and rate. A. Cross-section B1: the LH duplexes form sequentially with deformation in the Paro Window first and in the southern Baxa duplex second. A range of timing is explored with motion on the MCT and Paro Thrust over by 15 Ma (median age of LH monazite) or 12 Ma (youngest ages of monazite), and completion of duplex formation by 9 or 6 Ma. This version requires the slowest shortening rates from 9 or 6 Ma to 0 Ma. B. Cross-section B2: This section shows the Baxa duplex forming at the same time as the Paro window duplex, requiring that the Paro duplex is comprised of only Daling–Shumar Group horses. The Paro duplex is composed of forward dipping horses, which keeps the youngest active uplift in the north to match the trend of ZHe ages that young from S to N (9 Ma to 6 Ma). C. Cross-section B3: Similar geometry to section B2, however post formation, the Paro window slides along a Daling–Shumar Group flat to move the active ramp northward under the Lingshi klippe. The predicted ages for constant shortening rates (from 9 Ma to present) are shown in the parentheses with a (k) subscript. (For interpretation of the references to color in this figure legend, the reader is referred to the web version of this article.)

Table 2
Shortening and shortening rate data for deformation increments.

Deformation increment	Incremental shortening	Total shortening	Time range	Support	Possible rates	Integrated rates
Scenario A						
1	0	0	26 to 20.8 ± 1.1 Ma	prograde monazite ages in GH rocks		
2	200 km	200 km	–			
3	87 km	287 km	20.8 ± 1.1 to 15 ± 2.4 Ma, (a) end at 12 Ma, (b) end at 15 Ma	prograde monazite age in LH rocks	36 mm/yr (a), 54.7 mm/yr (b)	15–6 Ma (ST – duplex) 21.5 mm/yr (c)
4	80 km	367 km	15 ± 2.4 Ma to 9 Ma, (∗) 15–12 Ma, (a) 12–10.5 Ma, (b) 15–10.5 Ma	ZHe cooling in ST hanging wall and in the Paro duplex indicates latest age for motion on ST at 9 Ma	26.3 mm/yr (∗), 52.6 mm/yr (a), 17.5 mm/yr (b)	15–9 Ma (ST – duplex) 32.3 mm/yr (d)
5	74 km	441 km				
6	40 km	481 km	9 Ma (b) or 6 Ma (a)	9–6 Ma ZHe cooling ages in Paro Window and Baxa duplex	25.5 mm/yr (a), 76 mm/yr (b)	12–6 Ma (ST–duplex) 32.3 mm/yr (e)
7	34 km	515 km	9 or 6 Ma to present		5.6 mm/yr (a), 3.7 (b)	12–9 Ma (ST–duplex) 64.6 mm/yr (f)
			9–2 Ma	(partitioning last increment of shortening between 9–2 and 2–0 Ma)	2.8 mm/yr	
			2–0 Ma		9.5 mm/yr	
Scenario B						
1			26 to 20.8 ± 1.1 Ma	prograde monazite ages in GH rocks		
2	220 km	220 km				
3	140 km	360 km	20 to 12 Ma	youngest prograde monazite age in LH rocks	45 mm/yr (g)	
4	80 km	440 km	12–9 Ma	9 Ma ZHe cooling age in ST hanging wall	26.6 mm/yr (g)	44 mm/yr (h) combined MCT, PT and ST: 20 Ma to 9 Ma
5	–	–				
6	84 km	524 km	9–6 Ma	youngest ZHe cooling ages cap	28 mm/yr (g)	13.7 mm/yr (h): 9 Ma to 0 Ma
7	40 km	564 km	6–0 Ma	duplex growth	6 mm/yr (g)	
Scenario C						
1			26 to 20.8 ± 1.1 Ma	prograde monazite ages in GH rocks		
2	205 km	205 km				
3	87 km	292 km	20.8 ± 1.1 to 15 ± 2.4 Ma, (i) 12 Ma, (j) 15 Ma,	youngest prograde monazite age in LH rocks	36.5 mm/yr (i), 58.4 mm/yr (j)	31–37 mm/yr (k) combined MCT, PT and ST 20–9 Ma
4	80 km	372 km	15–9 Ma (j) or 12–9 Ma (i)	9 Ma ZHe cooling age in ST hanging wall	26.6 mm/yr (i), 13.3 mm/yr (j)	
5	74 km	446 km			38 mm/yr (i, j)	18.5 mm/yr constant rate 9–0 Ma (k)
6	40 km	486 km	end at 6 Ma	youngest ZHe cooling ages cap	38 mm/yr (i, j)	
7	53 km	539 km	6–0 Ma	duplex growth	8 mm/yr (i, j)	

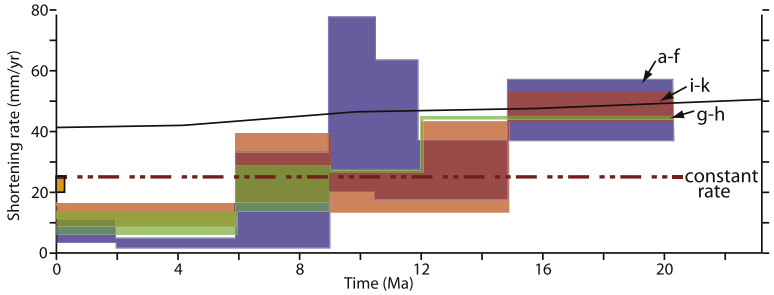

Fig. 4. Graph of horizontal shortening rate versus time illustrating variations in potential shortening rates explored in Fig. 3. The thin black line shows overall India–Asia convergence rate (from Copley et al., 2010). The yellow box shows range of GPS convergence rates for the eastern Himalayan thrust belt (~20–25 mm/yr Banerjee et al., 2008). The dark red (dash/dot) line shows the long-term average shortening rate between 20 and 0 Ma from western Bhutan data ($25+2/-1$ mm/yr). Range of permissible shortening rates from version 3A (a–f) are shown in blue, permissible rates from version 3B (g–h) are shown in red, and rates from version 3C (i–k) are shown in green. (For interpretation of the references to color in this figure legend, the reader is referred to the web version of this article.)

6. Discussion

6.1. Spatial patterns of cooling in western Bhutan

Although this paper has focused on cooling ages for a structural transect along the Wang Chu in western Bhutan, Fig. 1B also highlights important lateral variations in cooling history. The most noticeable variations are the young AFT ages extending along a N–S transect along the Puna Tsang Chu ~50 km to the east. Except for the southernmost sample F12, the AFT ages along the Puna Tsang Chu decrease northward from 5.3 Ma to 2.2 Ma (Fig. 1). This uniform trend in young AFT ages is markedly different from the cooling ages observed 50 km to the west along the Wang Chu, where there is no systematic trend in any chronometer. Along the Puna Tsang Chu AFT ages are consistent with transport of material over a northward migrating ramp (e.g., Long et al., 2012) at an integrated rate of 7–9 mm/yr over the last ~5 Myr.

The cooling ages (Fig. 2) illustrate structural and exhumational variability both along- and across-strike, over scales of 10's of kilometers, similar to results documented in recent studies in the western (Deeken et al., 2011) and eastern (Adlakha et al., 2012) parts of the Indian Himalaya. Structural variability is inferred from the need for mechanisms to explain these along- and across-strike changes. As proposed by Adlakha et al. (2012), the variability in cooling ages and rates across short distances (10–50 km) suggests that the pattern of exhumation is a response to differential rock uplift related to faulting. However, difficulty arises in explaining the lateral variations that we observe in western Bhutan using the traces of surface-breaking faults because the vertical component of fault-related exhumation must be large enough to reset AFT and possibly ZHe chronometers. Further, the lateral extent of hypothetical faulting in the Puna Tsang Chu cannot extend into the Paro window due to the lack of both young cooling ages and offset geologic boundaries (Fig. 1B). We suggest that rather than surface-breaking faults, it is the variability in the location and height of footwall ramps that control differential rock uplift. The along-strike extent of these structures is limited. Changing map patterns at the surface (such as the presence of the Paro window in Bhutan and the Sikkim half-window) must be accommodated by changing fault patterns at depth. A broad, N–S trending, regional syncline between western Bhutan and eastern Sikkim marks the lateral extent of the structures that comprise each of these duplex systems as well as subsurface lateral faults that allow the duplex systems to have different geometries, kinematics and possibly timing (Bhattacharyya and Mitra, 2009; Mitra et al., 2010). Fold–thrust belt ramp-flat geometry, as well as the location and kinematics of duplex systems, is directly related to the mechanical stratigraphy of rocks (Mitra and Boyer, 1986), which can change over length scales of 10's of kilometers. Thus the geometry of the basal decollement, which is best identified through geophysical studies, is only directly applicable to the region of observation. The potential for significant lateral variability emphasizes the importance of focused thermal models that do not cross lateral structures that mark significant changes in either footwall ramps or fault kinematics.

6.2. Comparisons and implications of spatial variations in shortening rates

Plotting the variation in shortening rates with time in western Bhutan highlights that there are windows of time when shortening approaches or equals plate convergence rates (Fig. 4), and that there has been a broad, general slowing of rates with time. Within error, rates of displacement on the MHT were at or near plate convergence rates from 20 to 9–6 Ma (Fig. 4). Thus the most noticeable change in rate is post 9 or 6 Ma when displacement on the MHT appears to have slowed to less than 10 mm/yr. The only way to increase shortening rates in this window of time is to assume constant shortening and duplex growth with minimal exhumation (Fig. $3_{h,k}$). The critical location for evaluating the range in rates that we explored in Fig. 3 is the exposed Baxa duplex in southwestern Bhutan. In this region we collected 9 samples for ZHe cooling ages. In the eastern section (Fig. 1), these cooling ages ($n=3$) are 9 Ma, including a sample taken from the immediate hanging wall of the MBT. In the western portion, three samples showed cooling younger than 3 Ma while three samples indicated minimal cooling post 6.0–8.6 Ma. These data were collected from three transects that exposed fairly continuous sections of LH rocks from the MCT to the southern range front. Constant rates of shortening, or cross-section kinematics that require significant shortening in these rocks from 6 Ma to present (Fig. 4C) must contend with the six ZHe cooling ages that are 6–9 Ma. A combination of more detailed mapping with more complete coverage of cooling ages could help elucidate the magnitude of permissible shortening in this region post 6 Ma. In addition, thermal advection models that predict cooling ages (e.g. Whipp et al., 2007; Herman et al., 2010) combined with the kinematics of cross-section deformation (Fig. 3) have the potential to differentiate between the likelihood of continued cooling post structural elevation gain (Fig. 3A5) or creation of structural elevation with minimal exhumation and cooling (Fig. $3B_h$, $C_{i,j,k}$).

The slower shortening rate post 9–6 Ma is similar to the change in rates identified in both eastern Bhutan (Long et al., 2012) and westernmost Nepal (Robinson and McQuarrie, 2012). A pronounced change in rate over an along-strike distance of greater than 1000 km suggests that the cause may be a function of how convergence is partitioned across the orogen rather than a result of local or regional deformation conditions. Although varying in time and location, ~13–8 Ma was a time of structural reorganization

of deformation on the Tibetan plateau, expressed as the onset of contractional deformation accompanied by strike-slip faulting (e.g., Taylor et al., 2003) and the outward growth of the northern and eastern parts of the plateau (e.g., Zheng et al., 2006; Craddock et al., 2011; Lease et al., 2011). However, combined shortening and cooling ages from NW India (Webb, 2013), immediately to the west of westernmost Nepal (Robinson and McQuarrie, 2012) suggests shortening rates of 18–19 mm/yr over the last 5 Myr.

Mismatch between GPS rates and the longer-term rate from 10 Ma to present requires a geologically recent acceleration of convergence rates sometime before the present. In eastern Bhutan a trend in ZHe ages from S to N along the Kuri Chu valley suggests a 9.6 mm/yr horizontal motion rate on the MHT between ~10 and 4 Ma, implying that an acceleration in shortening may have occurred within the last 4 Myr (Long et al., 2012). Along the Wang Chu transect in western Bhutan, increases in exhumation rates over the last 2 million years also suggest an acceleration in shortening. However, the magnitude of this acceleration is uncertain. An increase in shortening rates similar to geodetic rates is supported by offset and rotated Holocene markers that suggest rates of 23 ± 6.2 mm/yr over the 10 km-wide MFT zone in Arunachal Pradesh, India (Burgess et al., 2012). This rate would mark a return to the higher ~20–25 mm/yr GPS rates measured in the eastern Himalaya (Banerjee et al., 2008) by the Holocene. In contrast, Holocene slip rates of 9 ± 3 mm/yr have been calculated for the MFT in NW India (Wesnousky et al., 1999; Malik and Nakata, 2003; Kumar et al., 2006), slower than GPS shortening rates obtained across that region (Banerjee and Burgmann, 2002; Ponraj et al., 2011), but similar to the predicted rate of shortening from 10 Ma to present (Robinson and McQuarrie, 2012).

7. Conclusions

1. Published monazite ages combined with new and published MAr, ZHe, and AFT cooling ages from LH and GH rocks in western Bhutan highlight temporal variability in exhumation rates with most exhumation predating 9–6 Ma.

2. Peak exhumation occurred from ~13 to 9 Ma in the Paro window region with cooling rates in excess of 75 °C/Myr. Young, rapid exhumation with rates of 50–90 °C/Myr accompanied recent thrust faulting near the front of the range from ~2 Ma to present.

3. Linking pulses of rapid exhumation to the geometry of fold and thrust belt structure that evolves with time suggests periods of rapid shortening at rates close to India/Asia convergence rates (30–60 mm/yr), with the potential of shortening rates dramatically slowing in the last 9–6 Myr to an average of ~4–8 mm/yr. Young, rapid exhumation in the frontal part of the fold–thrust belt implies that the shortening rate could have increased again in the last 2 Myr. Constant shortening rates would require that minimal exhumation accompanied duplex growth from 9–6 Ma to present.

4. Variation in fold and thrust belt geometry, particularly the locations and magnitudes of footwall ramps, exerts first-order control on cooling patterns. This is best seen in the spatial variability of cooling histories over 10's of km distances. Permissible variations in cross-section geometry and kinematics change the predicted/permissible cooling history. Thus cooling ages have the potential to test the viability of proposed cross-section kinematics.

5. Youngest cooling ages may not mark the fastest thrusting rates or the window of fastest exhumation. Temporal variations in exhumation and the onset of rapid exhumation are best viewed through identifying transients in exhumation rate.

Acknowledgements

We would like to thank the government of Bhutan for their assistance and support, particularly the late Director General D. Wangda of the Department of Geology and Mines and the current Chief Geologist/Head U. Wangda of the Geological Survey of Bhutan in the Ministry of Economic Affairs. We especially acknowledge Isabelle Coutand and Djordje Grujic who collected many of the ZHe samples presented in this manuscript, and Uttam Chowdhury and Erin Abel from the University of Arizona Radiogenic Helium Dating Laboratory who prepared and analyzed the ZHe samples. John Lee of the USGS is thanked for his assistance with the Ar/Ar analyses. Alex Webb and an anonymous reviewer are thanked for their constructive comments that helped improve the manuscript. This work was primarily funded by NSF EAR 0738522 to N. McQuarrie.

Appendix A. Supplementary material

Supplementary material related to this article can be found online at http://dx.doi.org/10.1016/j.epsl.2013.10.045.

References

Adlakha, V.A., Lang, K.A., Patel, R.C., Lal, N., Huntington, K.W., 2012. Rapid long-term erosion in the rain shadow of the Shillong Plateau, Eastern Himalaya. Tectonophysics 582, 76–83. http://dx.doi.org/10.1016/j.tecto.2012.09.022.

Avouac, J.-P., 2003. Mountain building, erosion, and the seismic cycle in the Nepal Himalaya. Adv. Geophys. 46. http://dx.doi.org/10.1016/S0065-2687(03)46001-9.

Banerjee, P., Bürgmann, R., 2002. Convergence across the northwest Himalaya from GPS measurements. Geophys. Res. Lett. 29 (16), 52. http://dx.doi.org/10.1029/2002GL015184.

Banerjee, P., Bürgmann, R., Nagarajan, B., Apel, E., 2008. Intraplate deformation of the Indian subcontinent. Geophys. Res. Lett. 35, L18301. http://dx.doi.org/10.1029/2008GL035468.

Bettinelli, P., Avouac, J.-P., Flouzat, M., Jouanne, F., Bollinger, L., Willis, P., Chitrakar, G.R., 2006. Plate motion of India and interseismic strain in the Nepal Himalaya from GPS and DORIS measurements. J. Geod. 80, 567–589.

Bhattacharyya, K., Mitra, G., 2009. A new kinematic evolutionary model for the growth of a duplex – an example from the Rangit duplex, Sikkim Himalaya, India. Gondwana Res. 16, 697–715.

Bilham, R., Larson, K., Freymueller, J., 1997. Indo-Asian convergence rates in the Nepal Himalaya. Nature 311, 621–626.

Brandon, M.T., Roden-Tice, M.K., Garver, J.I., 1998. Late Cenozoic exhumation of the Cascadia accretionary wedge in the Olympic Mountains, northwest Washington State. Geol. Soc. Am. Bull. 110, 985–1009. http://dx.doi.org/10.1130/0016-7606(1998)110<0985:LCEOTC>2.3.CO.

Burgess, W.P., Yin, A., Dubey, C.S., Shen, Z.-K., Kelty, T.K., 2012. Holocene shortening across the Moain Frontal Thrust zone in the eastern Himalaya. Earth Planet. Sci. Lett. 357–358, 152–167.

Copley, A., Avouac, J.-P., Royer, J.-Y., 2010. India–Asia collision and the Cenozoic slowdown of the Indian plate: Implications for the forces driving plate motions. J. Geophys. Res. 115, B03410. http://dx.doi.org/10.1029/2009JB006634.

Craddock, W., Kirby, E., Zhang, H., 2011. Late Miocene–Pliocene range growth in the interior of the northeastern Tibetan Plateau. Lithosphere 3, 420–438. http://dx.doi.org/10.1130/L159.1.

Daniel, C.G., Hollister, L.S., Parrish, R.R., Grujic, D., 2003. Exhumation of the main central thrust from lower crustal depths, eastern Bhutan Himalaya. J. Metamorph. Geol. 21, 317–334. http://dx.doi.org/10.1046/j.1525-1314.2003.00445.x.

DeCelles, P.G., Robinson, D.M., Quade, J., Ojha, T.P., Garzione, C.N., Copeland, P., Upreti, B.N., 2001. Stratigraphy, structure, and tectonic evolution of the Himalayan fold–thrust belt in western Nepal. Tectonics 20, 487–509.

Deeken, A., Thiede, R.C., Sobel, E.R., Hourigan, J.K., Strecker, M.R., 2011. Erosional variability within the Himalaya of northwest India. Earth Planet. Sci. Lett. 305, 103–104.

Ehlers, T.A., Farley, K.A., 2003. Apatite (U–Th)/He thermochronometry; methods and applications to problems in tectonic and surface processes. Earth Planet. Sci. Lett. 206, 1–14.

Ehlers, T.A., Willett, S.D., Armstrong, P.A., Chapman, D.S., 2003. Exhumation of the Central Wasatch Mountains, Utah: 2. Thermo-kinematics of exhumation, erosion and thermochronometer interpretation. J. Geophys. Res. 108, 2173. http://dx.doi.org/10.1029/2001JB001723.

Farley, K.A., 2000. Helium diffusion from apatite: General behavior as illustrated by Durango flourapatite. J. Geophys. Res. 105, 2903–2914.

Gansser, A., 1964. Geology of the Himalaya. Wiley, Basel, pp. 1–289.

Gansser, A., 1983. Geology of the Bhutan Himalaya. Birkhäuser Verlag, Basel, Switzerland. 181 pp.

Gehrels, G.E., Kapp, P., DeCelles, P.G., Pullen, A., Blakey, R., Weislogel, A., Ding, L., Guynn, J., Martin, A., McQuarrie, N., Yin, A., 2011. Detrital zircon geochronology

of pre-Tertiary strata in the Tibetan–Himalayan orogeny. Tectonics 30, TC5016. http://dx.doi.org/10.1029/2011TC002868.
Grujic, D., Coutand, I., Bookhagen, B., Bonnet, S., Blythe, A., Duncan, C., 2006. Climatic forcing of erosion, landscape, and tectonics in the Bhutan Himalayas. Geology 34, 801–804.
Grujic, D., Warren, C.J., Wooden, J.L., 2011. Rapid synconvergent exhumation of Miocene-aged lower orogenic crust in the eastern Himalaya. Lithosphere 3, 346–366. http://dx.doi.org/10.1130/L154.1.
Hames, W.E., Bowring, S.A., 1994. An empirical evaluation of the argon diffusion geometry in muscovite. Earth Planet. Sci. Lett. 124, 161–167.
Harrison, T.M., Celerier, J., Ailkman, A.B., Hermann, J., Heizler, M., 2009. Diffusion of Ar^{40} in muscovite. Geochim. Cosmochim. Acta 73, 1039–1051. http://dx.doi.org/10.1016/j.gca.2008.09.038.
Hauck, M.L., Nelson, K.D., Brown, W., Zhao, W., Ross, A.R., 1998. Crustal structure of the Himalayan orogen at 90°E longitude from Project INDEPTH deep reflection profiles. Tectonics 17, 481–500. http://dx.doi.org/10.1029/98TC01314.
Herman, F., Copeland, P., Avouac, J.-P., Bollinger, L., Mahéo, G., Le Fort, P., Rai, S., Foster, D., Pêcher, A., Stuwe, K., Henry, P., 2010. Exhumation, crustal deformation, and thermal structure of the Nepal Himalaya derived from the inversion of thermo-chronological and thermobarometric data and modeling of the topography. J. Geophys. Res. 115, B06407. http://dx.doi.org/10.1029/2008JB006126.
Hodges, K.V., 2000. Tectonics of the Himalayas and southern Tibet from two perspectives. Geol. Soc. Am. Bull. 112, 324–350.
Hollister, L.S., Crawford, M.L., 1986. Melt-enhanced deformation: A major tectonic process. Geology 14, 558–561. http://dx.doi.org/10.1130/0091-7613(1986)14<558:MDAMTP>2.0.CO.
Kellett, D.A., Grujic, D., Warren, C., Cottle, J., Jamieson, R., Tenzin, T., 2010. Metamorphic history of a syn-convergent orogen-parallel detachment: the South Tibetan Detachment system, Bhutan Himalaya. J. Metamorph. Geol. 28, 785–808.
Kirschner, D.L., Cosca, M.A., Masson, H., Hunziker, J.C., 1996. Staircase $^{40}Ar/^{39}Ar$ spectra of fine grained while mica: timing and duration of deformational and empirical constraints on argon diffusion. Geology 24, 747–750.
Kohn, M.J., 2008. *P–T–t* data from central Nepal support critical taper and repudiate large-scale channel flow of the Greater Himalayan sequence. Geol. Soc. Am. Bull. 120, 259–273. http://dx.doi.org/10.1130/B26252.1.
Kohn, M.J., Malloy, A.M., 2004. Formation of monazite via prograde metamorphic reactions among common silicates: implications for age determinations. Geochim. Cosmochim. Acta 68, 101–113.
Kohn, M.J., Wieland, M.S., Parkinson, C.D., Upreti, B.N., 2004. Miocene faulting at plate tectonic velocity in the central Himalaya, Nepal. Earth Planet. Sci. Lett. 228, 299–310.
Kohn, M.J., Wieland, M.S., Parkinson, C.D., Upreti, B.N., 2005. Five generations of monazite in Langtang gneisses: implications for chronology of the Himalayan metamorphic core. J. Metamorph. Geol. 23, 399–406.
Kumar, S., Wesnousky, S.G., Rockwell, T.K., Briggs, R.W., Thakur, V.C., Jayangondaperumal, R., 2006. Paleoseismic evidence of great surface rupture earthquakes along the Indian Himalaya. J. Geophys. Res. 111, B03304. http://dx.doi.org/10.1029/2004JB003309.
Larson, K.M., Burgmann, R., Bilham, R., Freymueller, J., 1999. Kinematics of the India–Eurasia collision zone from GPS measurements. J. Geophys. Res. 104, 1077–1093.
Laslett, G.M., Green, P.F., Duddy, I.R., Gleadow, A.J.W., 1987. Thermal annealing of fission tracks in apatite: 2. A quantitative analysis. Chem. Geol. 65, 1–13. http://dx.doi.org/10.1016/0168-9622(87)90057-1.
Lavé, J., Avouac, J.P., 2000. Active folding of fluvial terraces across the Siwaliks Hills, Himalayas of central Nepal. J. Geophys. Res. 105 (B3), 5735–5770.
Lease, R.O., Burbank, D.W., Clark, M.K., Farley, K.A., Zhang, D., Zhang, H., 2011. Middle Miocene reorganization of deformation along the northeastern Tibetan Plateau. Geology 39, 359–362. http://dx.doi.org/10.1130/G31356.1.
LeFort, P., 1975. Himalayas: the collided range. Present knowledge of the continental arc. Am. J. Sci. 275-A, 1–44.
Long, S., McQuarrie, N., Tobgay, T., Grujic, D., Hollister, L., 2011a. Geologic map of Bhutan. J. Maps 2011, 184–192. 1:500,000-scale, http://dx.doi.org/10.4113/jom.2011.1159.
Long, S., McQuarrie, N., Tobgay, T., Grujic, D., 2011b. Geometry and crustal shortening of the Himalayan fold–thrust belt, eastern and central Bhutan. Geol. Soc. Am. Bull. 123, 1427–1447. http://dx.doi.org/10.1130/B30203.1.
Long, S.P., McQuarrie, N., Tobgay, T., Coutand, I., Cooper, F., Reiners, P., Wartho, J., Hodges, K.V., 2012. Variable shortening rates in the eastern Himalayan thrust belt, Bhutan: insights from multiple thermochronologic and geochronologic datasets tied to kinematic reconstructions. Tectonics 31, TC5004. http://dx.doi.org/10.1029/2012TC003155.
Lyon-Caen, H., Molnar, P., 1985. Gravity anomalies, flexure of the Indian plate, and the structure, support and evolution of the Himalaya and Ganga Basin. Tectonics 4, 513–538. http://dx.doi.org/10.1029/TC004i006p00513.
Malik, J.N., Nakata, T., 2003. Active faults and related late quaternary deformation along the northwestern Himalayan Frontal Zone, India. Ann. Geophys. 46, 917–936.
Mancktelow, N.S., Grasemann, B., 1997. Time-dependent effects of heat advection and topography on cooling histories during erosion. Tectonophysics 270, 167–195. http://dx.doi.org/10.1016/S0040-1951(96)00279-X.
McQuarrie, N., Robinson, D., Long, S.P., Tobgay, T., Grujic, D., Gehrels, G., Ducea, M., 2008. Preliminary stratigraphic and structural architecture of Bhutan: Implications for the along-strike architecture of the Himalayan system. Earth Planet. Sci. Lett. 272, 105–117. http://dx.doi.org/10.1016/j.epsl.2008.04.030.
McQuarrie, N., Long, S.P., Tobgay, T., Nesbit, J.N., Gehrels, G., Ducea, M., 2013. Documenting basin scale, geometry and provenance through detrital geochemical data: lessons from Neoproterozoic to Ordovician strata of Bhutan. Gondwana Res. 23, 1491–1510. http://dx.doi.org/10.1016/j.gr.2012.09.002.
Mitra, G., Boyer, S.E., 1986. Energy balance and deformation mechanisms of duplexes. J. Struct. Geol. 8, 291–304.
Mitra, G., Bhattacharyya, K., Mukul, M., 2010. The lesser Himalayan Duplex in Sikkim: Implications for variations in Himalayan shortening. J. Geol. Soc. India 75 (1), 289–301. http://dx.doi.org/10.1007/s12594-010-0016-x.
Mitra, S., Priestley, K., Bhattacharyya, A.K., Gaur, V.K., 2005. Crustal structure and earthquake focal depths beneath northeasteern India and southern Tibet. Geophys. J. Int. 160, 227–248.
Naeser, N.D., Naeser, C.W., McCulloh, T.H., 1989. The application of fission-track dating to depositional and thermal history of rocks in sedimentary basins. In: Naeser, N.D., McCulloh, T.H. (Eds.), Thermal History of Sedimentary Basins – Methods and Case Histories. Springer-Verlag, New York, pp. 157–180.
Ni, J., Barazangi, M., 1984. Seismotectonics of the Himalayan collision zone: Geometry of the underthrusting Indian plate beneath the Himalaya. J. Geophys. Res. 89, 1147–1164. http://dx.doi.org/10.1029/JB089iB02p01147.
Parrish, R.R., 1983. Cenozoic thermal evolution and tectonics of the coast mountains of British Columbia 1. Fission track dating apparent uplift rates, and patterns of uplift. Tectonics 2, 601–631.
Ponraj, M., Miura, S., Reddy, C.D., Amirtharaj, S., Mahajan, S.H., 2011. Slip distribution beneath the Central and Western Himalaya inferred from GPS observations. Geophys. J. Int. 185, 724–736. http://dx.doi.org/10.1111/j.1365-246X.2011.04958.x.
Pyle, J.M., Spear, F.S., 2003. Four generations of accessory-phase growth in low-pressure migmatites from SW New Hampshire. Am. Mineral. 88, 338–351.
Pyle, J.M., Spear, F.S., Rudnick, R.L., McDonough, W.F., 2001. Monazite–xenotime–garnet equilibrium in metapelites and a new monazite–garnet thermometer. J. Petrol. 42, 2083–2107.
Ray, L., Bhattacharya, A., Roy, S., 2007. Thermal conductivity of Higher Himalayan Crystallines from Garhwal Himalaya, India. Tectonophysics 434, 71–79. http://dx.doi.org/10.1016/j.tecto.2007.02.003.
Reiners, P.W., Spell, T.L., Nicolescu, S., Zanetti, K.A., 2004. Zircon (U–Th)/He thermochronometry: He diffusion and comparison with $^{40}Ar/^{39}Ar$ dating. Geochim. Cosmochim. Acta 68, 1857–1887.
Reiners, P.W., Ehlers, T.A., Zeitler, P.K., 2005. Past, present, and future of thermochronology. In: Reiners, P.W., Ehlers, T.A. (Eds.), Low-Temperature Thermochronology: Techniques, Interpretations, and Applications. In: Rev. Mineral. Geochem., vol. 58, pp. 1–18.
Robinson, D.M., McQuarrie, N., 2012. Pulsed deformation and variable slip rates in the Central Himalayan Thrust Belt. Lithosphere 4, 449–464. http://dx.doi.org/10.1130/L204.1.
Schulte-Pelkum, V., Monsalve, G., Sheehan, A., Pandey, M., Sapkota, S., Bilham, R., 2005. Imaging the Indian subcontinent beneath the Himalaya. Nature 425, 1222–1225.
Spear, F.S., Pyle, J.M., 2002. Apatite, monazite and xenotime in metamorphic rocks. Rev. Mineral. Geochem. 48, 293–335.
Spear, F.S., Kohn, M.J., Cheney, J.T., 1999. *P–T* paths from anatectic pelites. Contrib. Mineral. Petrol. 134, 17–32.
Taylor, M., Yin, A., Ryerson, F.J., Kapp, P., Ding, L., 2003. Conjugate strike-slip faulting along the Bangong–Nujiang suture zone accommodates coeval east–west extension and north–south shortening in the interior of the Tibetan Plateau. Tectonics 22, 1044. http://dx.doi.org/10.1029/2002TC001361.
Thiede, R., Ehlers, T.A., Bookhagen, B., Strecker, M.R., 2009. Erosional variability along the northwest Himalayan Front. J. Geophys. Res., Earth Surf. 114, F01015. http://dx.doi.org/10.1029/2008JF001010.
Tobgay, T., Long, S., McQuarrie, N., Ducea, M., Gehrels, G., 2010. Using isotopic and chronologic data to fingerprint strata: the challenges and benefits of variable sources to tectonic interpretations, the Paro Formation, Bhutan Himalaya. Tectonics 29, TC6023. http://dx.doi.org/10.1029/2009TC002637.
Tobgay, T., McQuarrie, N., Long, S.P., Kohn, M.J., Corrie, S.L., 2012. The age and rate of displacement along the Main Central Thrust in the western Bhutan Himalaya. Earth Planet. Sci. Lett. 319–320, 146–158. http://dx.doi.org/10.1016/j.epsl.2011.12.005.
Tshering, P., 2007. Detrital Muscovite in two drainage basins in western Bhutan (Masters Thesis). Massachusetts Institute of Technology, Boston, Mass. 83 pp.
Warren, C.J., Grujic, D., Cottle, J., Rogers, N.W., 2012. Constraining cooling histories: Rutile and titanite chronology and diffusion modeling in NW Bhutan. J. Metamorph. Geol. 30, 113–130. http://dx.doi.org/10.1111/j.1525-1314.2011.00958.x.
Webb, A.A.G., 2013. Preliminary palinspastic reconstruction of Cenozoic deformation across the Himachal Himalaya (northwestern India). Geosphere 9, 572–587. http://dx.doi.org/10.1130/GES00787.1.

Wesnousky, S.G., Kumar, S., Mohindra, R., Thakur, V.C., 1999. Uplift and convergence along the Himalayan Frontal Thrust of India. Tectonics 18, 967–976.

Whipp, D.M., Ehlers, T.A., Blythe, A.E., Huntington, K.W., Hodges, K.V., Burbank, D.W., 2007. Plio-quaternary exhumation history of the central Nepalese Himalaya: 2. Thermokinematic and thermochronometer age prediction model. Tectonics 26, TC3003. http://dx.doi.org/10.1029/2006TC001991.

Wing, B.N., Ferry, J.M., Harrison, T.M., 2003. Prograde destruction and formation of monazite and allanite during contact and regional metamorphism of pelites: petrology and geochronology. Contrib. Mineral. Petrol. 145, 228–250.

Wu, C., Nelson, K., Wortman, G., Samson, S., Yue, Y., Li, L., Kidd, W., Edward, M., 1998. Yadong cross structure and the South Tibetan Detachment in the east central Himalaya (89°–90°E). Tectonics 17, 28–45.

Yin, A., 2006. Cenozoic tectonic evolution of the Himalayan orogen as constrained by along-strike variation of structural geometry, exhumation history, and foreland sedimentation. Earth-Sci. Rev. 76, 1–131. http://dx.doi.org/10.1016/j.earscirev.2005.05.004.

Zhang, P., Shen, Z., Wang, M., Gan, W., Bürgmann, R., Molnar, P., 2004. Continuous deformation of the Tibetan Plateau from global positioning system data. Geology 32, 809–812.

Zheng, D., Zhang, P.Z., Wan, J.L., Yuan, D.Y., Li, C.Y., Yin, G.M., Zhang, G.L., Wang, Z.C., Min, W., Chen, J., 2006. Rapid exhumation at ~8 Ma on the Liupan Shan thrust fault from apatite fission-track thermochronology: Implications for growth of the northeastern Tibetan Plateau margin. Earth Planet. Sci. Lett. 248, 198–208. http://dx.doi.org/10.1016/j.epsl.2006.05.023.